Manngård, Mikael; Koene, Ivar; Lund, Wictor; Haikonen, Sampo; Fagerholm, Fredrik A.; Wilczek, Michał; Mnich, Konrad; Keski-Rahkonen, Joni; Viitala, Raine; Björkqvist, Jerker; Toivonen, Hannu T.

Torque estimation in marine propulsion systems

Published in:
Mechanical Systems and Signal Processing

DOI:
10.1016/j.ymssp.2022.108969

Published: 01/06/2022

Document Version
Publisher's PDF, also known as Version of record

Mechanical Systems and Signal Processing 172 (2022) 108969

Contents lists available at ScienceDirect

Mechanical Systems and Signal Processing

journal homepage: www.elsevier.com/locate/ymssp

Torque estimation in marine propulsion systems

Mikael Manngård [a,*], Ivar Koene [b], Wictor Lund [a], Sampo Haikonen [b], Fredrik A. Fagerholm [c], Michał Wilczek [c], Konrad Mnich [c], Joni Keski-Rahkonen [c], Raine Viitala [b], Jerker Björkqvist [a], Hannu T. Toivonen [a]

[a] Faculty of Science and Engineering, Åbo Akademi Univeristy, Vesilinnantie 3, 20500 Turku (Åbo), Finland
[b] Department of Mechanical Engineering, Aalto University, Sähkömiehentie 4P, PL 14400, 00076, Aalto, Finland
[c] Kongsberg Maritime Finland, Suojantie 5, 26100 Rauma, Finland

ARTICLE INFO

Communicated by E. Chatzi

Keywords:
Simultaneous input and state estimation
Optimal filtering
Maritime systems

ABSTRACT

An augmented Kalman filter for torque estimation in marine propulsion-system drive trains is presented. Propeller and motor excitations and torque responses are estimated based on a dynamical model of the system and inboard shaft measurements. Input excitations affecting marine propulsion systems are signals whose statistical properties vary between finite time intervals. Hence, in this paper, excitations are characterized as quasi-stationary signals with bounded power spectral density. Given that upper bounds on the spectral densities are known prior to estimation, it is shown that a linear time-invariant input-and-state observer, minimizing the worst-case power of the estimation errors, can be synthesized by conventional Kalman-filtering techniques. Experiments have been conducted on a laboratory-scale test bench to assess the applicability of the proposed observer for use in marine propulsion systems. The test bench was built to emulate the behavior of a full-scale propulsion system operated in ice and other high load conditions. Estimation results from a full-size underwater mountable azimuthing thruster are also presented. Experiment results show that torque excitations and torque responses at all locations of interest on the engine-propeller drivetrain can be estimated with high accuracy based on a few indirect measurements at convenient locations on the motor shaft.

1. Introduction

Marine propulsion systems should be designed to operate reliably and safely in varying load conditions. Responsible shipping in ice-covered seas is of increasing importance as maritime transport in the Arctic and Baltic regions is expected to increase [1,2]. A primary cause of component wear in propulsion-system drivetrains is excitations acting on the propeller. Especially propeller-ice interactions causing component wear and fatigue is a concern [2,3]. Although maritime industries have a long experience of applying torsional vibration analysis and dynamical modeling for the design of propulsion systems [4–7], and components are designed such that resonance at the operationally critical angular velocities are avoided, the actual wear on components during operation is unknown. Hence, the importance of monitoring loads in real-time, and their effects on the remaining useful lifetime of components, cannot be underestimated.

Although propeller ice-load excitations are described in the existing research literature [2,3,8–12] and in ice-class standards [13, 14], the exact dynamic nature of propeller-ice interactions and their effect on component wear and fatigue is currently not fully

* Corresponding author.
E-mail address: mikael.manngard@abo.fi (M. Manngård).

https://doi.org/10.1016/j.ymssp.2022.108969
Received 3 August 2021; Received in revised form 15 February 2022; Accepted 17 February 2022
Available online 3 March 2022

understood. Measuring the torque response of each component on the driveline is not only impractical due to the high installation cost, but may also be physically impossible due to design limitations. A more sustainable solution would be to estimate the excitations and torque responses based on a dynamical model and a few inline measurements at convenient locations on the drivetrain.

Estimation of propeller-ice moments based on inboard shaft measurements has been studied in [2,3] by the use of a dynamical model and the solution of a regularized inverse problem. In [15] an augmented Kalman filter (AKF) using a random-walk excitation model was proposed for propeller-torque estimation in azimuthing thrusters. In this paper, the AKF framework is extended to input excitations belonging to the class of quasi-stationary signals [15]. The filter is worst-case optimal with respect to assumed upper bounds on the spectra of the unknown inputs. By formulating the problem as a simultaneous input-and-state estimation problem (SISE), the torque responses in the system can be estimated in addition to the unknown propeller (and motor) loads. Measurement errors can also be accounted for naturally in the AKF framework, which is a clear benefit compared to the inverse-problem formulations.

The problem of state estimation with unknown input signals has generated great interest since it was originally introduced in [16–18]. Simultaneous input and state estimation for completely unknown input signals was the main focus of [16], and the results have been further analyzed and refined since then [19–22]. In [23] a connection between the SISE estimator [19] and the Kalman filter was established.

Another commonly used approach, which has shown promising results in practice, is to design a Kalman filter based on a system model augmented with simple input models. Augmented Kalman filters have been applied for load and force estimation in mechanical structures, see, e.g., [24,25]. An unscented Kalman filter for input-parameter-state estimation was presented in [26] and numerical examples of estimation of inputs, responses, and stiffness and damping parameters were provided. In [27] optimal sensor placement for input estimation using augmented Kalman filters was studied. In [15] the performance of an augmented Kalman filter for torque estimation in azimuth thrusters was evaluated on a simulation study.

Torque estimation has also been studied within the automotive industry. For example, to mention a few, in [28] the problem of estimating periodic combustion torques in an automotive engine using engine-speed measurements was studied, and in [29] the combustion torque in a diesel engine was estimated from angular velocity measurements from the crankshaft. In [29], it was stated that colored white noise could be a good representation of the combustion torque. This bears a resemblance to what was proposed in [15] for propeller torque excitations. In this paper, instead of modeling torque excitations in terms of colored noise, excitations are characterized as quasi-stationary signals.

Results on torque and load estimation in marine propulsion systems have not yet been presented in the existing literature. Thus, in this paper, the problem of torque estimation in marine propulsion systems is studied. We show that an optimal time-invariant input-and-state observer, minimizing the worst-case power of the estimation error, can be realized as an augmented Kalman filter and synthesized based on an upper bound on the spectral densities of the unknown input signals. The performance of the proposed input-and-state observer is evaluated on a laboratory-scale test bench of a propulsion system. Experiments on the test bench were designed to mimic on-sea conditions of a two-gear azimuth thruster operated in ice-load conditions. Estimation results from a full-size azimuthing thruster in operation are also presented.

The paper is structured as follows. In Section 2 a dynamical model of an azimuth-thruster driveline is presented, and in Section 3 a characterization of unknown input signals is provided. In Section 4 the simultaneous input-and-state estimation problem is formulated, and an optimal time-invariant input-and-state observer is derived. In Section 5 the performance of the proposed estimator is evaluated on a laboratory-scale test bench, and in Section 6 estimation results from a sea trial are presented.

1.1. Main contributions

The main contributions of this paper are three-fold:

(i) Unknown input excitations affecting marine propulsion systems are characterized by a class of quasi-stationary signals with bounded spectral density.
(ii) An optimal worst-case linear time-invariant input-and-state observer assuming spectral bounds on the unknown input signals is synthesized using conventional Kalman-filtering techniques.
(iii) Experiment results indicate that unknown torque excitations and torque responses at all locations on the drivetrain can be estimated with high accuracy based on a limited number of measurements at convenient locations on the input shaft.

2. System description

An L-drive underwater mountable azimuth thruster consists of a vertically mounted motor with a shaft connecting to a gear via a flexible coupling, which, in turn, connects to the propeller, cf. Fig. 1(a). In this section, a dynamical model of the propulsion system is presented. A continuous-time model of the drivetrain is derived using first principles and is converted into a discrete-time state–space model used for synthesizing the input-and-state observer.

To simulate and analyze torsional vibrations in rotating machinery, structures are often represented by lumped-mass spring–damper systems [15,30,31]. A lumped-mass model of an azimuth-thruster drivetrain is illustrated in Fig. 1(b). As in [15], components $i = 1, 2, \dots, N$ on a marine thruster driveline are modeled by a set of lumped masses with mass moment of inertia I_i. The torsional

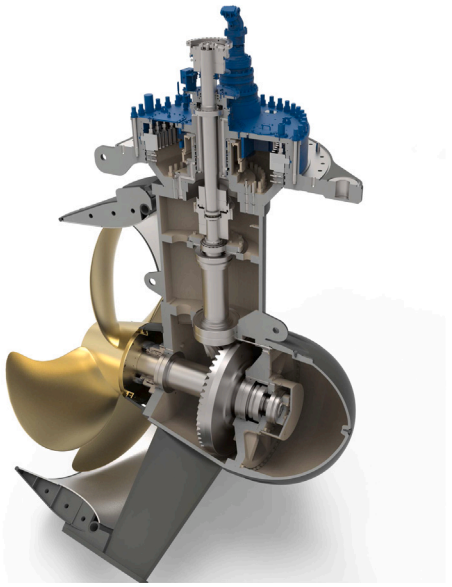

(a) Underwater mountable azimuthing thruster.

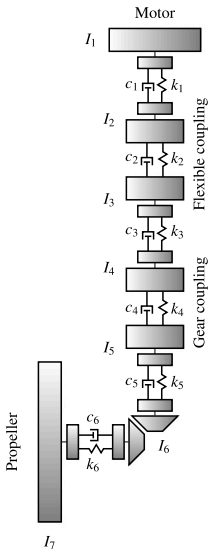

(b) Lumped-mass model of an azimuth thruster driveline.

Fig. 1. (a) Cutaway diagram of an azimuth thruster. (b) Lumped mass model of an azimuth thruster.

angle at the ith lumped mass is denoted $\theta_i(t)$, the angular velocity $\dot{\theta}_i(t) = \frac{\mathrm{d}}{\mathrm{d}t}\theta(t)$, and the angular deflection (twist) between lumped masses are denoted $\Delta\theta_i(t) = n_i\theta_i(t) - \theta_{i+1}(t)$, where the gear-ratio n_i between the ith and $i+1$th mass is defined as

$$n_i = \frac{\theta_{i+1}(t)}{\theta_i(t)} = \frac{\dot{\theta}_{i+1}(t)}{\dot{\theta}_i(t)}.$$

Gears are assumed ideal. A more detailed description of how to convert ideal gears into equivalent single lumped masses is, for example, to be found in [32, Ch. 2] and [15].

The torsional motion of the lumped-mass system is derived from conservation laws. The angular velocity of the ith lumped mass is given by

$$I_i\ddot{\theta}_i(t) = c_{i-1}\left(n_{i-1}\dot{\theta}_{i-1}(t) - \dot{\theta}_i(t)\right) - c_i n_i\left(n_i\dot{\theta}_i(t) - \dot{\theta}_{i+1}(t)\right) - d_i\dot{\theta}_i(t) + k_{i-1}\Delta\theta_{i-1}(t) - k_i n_i\Delta\theta_i(t),\ i = 2,\dots,N-1 \tag{1}$$

where c_i are damping factors, k_i is the stiffness coefficient, and terms $-d_i\dot{\theta}_i(k)$ are the torque lost by absolute damping caused by e.g. internal friction in the system. The angular velocity of the component closest to the motor is given by

$$I_1\ddot{\theta}_1(t) = -c_1 n_1\left(n_1\dot{\theta}_1(t) - \dot{\theta}_2(t)\right) - d_1\dot{\theta}_1(t) - k_1\Delta\theta_1(t) + u_{\mathrm{m}}(t), \tag{2}$$

where $u_{\mathrm{m}}(k)$ is the motor torque, and the angular velocity of the propeller is

$$I_N\ddot{\theta}_N(t) = c_{N-1}\left(n_{N-1}\dot{\theta}_{i-1}(t) - \dot{\theta}_i(t)\right) - d_N\dot{\theta}_i(t) + k_{N-1}\Delta\theta_{N-1}(t) + u_{\mathrm{p}}(t), \tag{3}$$

where $u_{\mathrm{p}}(k)$ is the propeller torque. The torsional twists are given by

$$\Delta\dot{\theta}_i(t) = \dot{\theta}_{i-1}(t) - \dot{\theta}_i(t),\ i = 1,\dots,N-1. \tag{4}$$

The continuous-time linear time-invariant system (1)–(3) can be expressed in state–space form

$$\dot{x}(t) = A_{\mathrm{c}}x(t) + B_{\mathrm{c}}u(t), \quad y(t) = C_{\mathrm{c}}x(t), \tag{5}$$

with vector of measurements $y(t) \in \mathbb{R}^p$, input vector $u(t) \in \mathbb{R}^2$, and state vector $x(t) \in \mathbb{R}^{2N-1}$ given by

$$u(t) = \begin{bmatrix} u_{\mathrm{m}}(t) \\ u_{\mathrm{p}}(t) \end{bmatrix},\ x(t) = \begin{bmatrix} \dot{\theta}_1(t) \\ \vdots \\ \dot{\theta}_N(t) \\ n_1\theta_1(t) - \theta_2(t) \\ \vdots \\ n_{N-1}\theta_{N-1}(t) - \theta_N(t) \end{bmatrix}.$$

The structure of system matrices A_c, B_c is presented in Appendix A. The matrix C_c is defined by which states (or linear combination of states) are measured. For example, a torque $\tau_i(t)$ caused by angular deflection between the ith and $(i+1)$th lumped masses can be modeled as

$$\tau_i(t) = k_i \Delta\theta_i(t). \tag{6}$$

Since $\tau_i(t)$ is a linear combination of states, C_c can be defined in such a way that torque measurements can be included in $y(t)$. Likewise, since angular velocities have been defined as states of the systems, angular velocity measurements can be included in $y(t)$.

In practice, measurements are typically obtained at discrete time instance $t = kT_s$, where the time index $k = 0, 1, \ldots$ and T_s is the sampling time. The vector of measurements at time instance k is modeled as

$$y(k) = Cx(k) + v_y(k),$$

where $v_y(k)$ is measurement noise.

Discretizing system (5) with respect to a constant sampling rate, the system can be expressed as a linear discrete-time invariant system of the form

$$\begin{aligned} x(k+1) &= Ax(k) + Bu(k) + Fv(k) \\ y(k) &= Cx(k) + Dv(k). \end{aligned} \tag{7}$$

The system is defined by matrices $A \in \mathbb{R}^{n\times n}$, $B \in \mathbb{R}^{n\times m}$, $F \in \mathbb{R}^{n\times n+p}$, $C \in \mathbb{R}^{p\times n}$ and $D \in \mathbb{R}^{p\times n+p}$, where $n = 2N-1$ is number of states and $m = 2$ the number of inputs. The vector $v(k) \in \mathbb{R}^{n+p}$ contains process noise $v_x(k) \in \mathbb{R}^n$ and measurement noise $v_y(k) \in \mathbb{R}^p$ with covariance matrices Q and R respectively. The noise vectors $v_x(k)$, $v_y(k)$ and input vector $u(k)$ are assumed to be uncorrelated. Without loss of generality, $v(k)$ can be defined to have unit covariance matrix by replacing F and D with matrices $F' = FV$ and $D' = DV$ respectively, where $V = \mathrm{diag}(Q^{1/2}, R^{1/2})$

There are no known physical sources of process noise in this case study. However, since it is the standard convention to include process noise in the model, and the Kalman-filtering framework presented in Section 4 can account for such, process noise was included in (7). The process noise can also be interpreted as uncertainty in the state of a system. It is natural to assume that uncertainties in the states $x(k)$ derived from (1)–(3) are larger than those derived from (4). Hence, F is set such that process noise $v_x(k)$ only affects angular velocities.

The main goal in this case study is to estimate the input excitations $u(k)$, as well as torque responses $\tau_i(k) = k_i\Delta\theta_i(k)$ at all lumped masses on the drive train. Since torque can be expressed as linear combinations of states, the vector to be estimated is defined as

$$z(k) = \begin{bmatrix} u(k-1) \\ Tx(k) \end{bmatrix} \in \mathbb{R}^r, \tag{8}$$

where T is a matrix defining which linear combination of states to be estimated. The estimated signal $z(k)$ contains the most recent state $x(k)$ and input $u(k-1)$ which affects the measurement $y(k)$ at time k. If, for example, all torque responses (6) are to be estimated, T would be an $(N-1)$-by-n matrix

$$T = \left[\begin{array}{c|c} 0 & T_1 \end{array}\right] = \left[\begin{array}{ccc|ccc} 0 & \cdots & 0 & k_1 & & \\ \vdots & \ddots & \vdots & & \ddots & \\ 0 & \cdots & 0 & & & k_{N-1} \end{array}\right].$$

3. Characterization of input signals

In conventional Kalman filtering, the unknown disturbances are assumed to be stationary stochastic signals. However, this assumption does not provide a satisfactory signal description in marine propulsion systems. Although it is fair to assume that process and measurement noise are stationary and stochastic, it is not wholly satisfactory to treat unknown input torques $u(k)$ as such. Unknown torque excitations affecting a propeller are caused by deterministic events such as sudden angular velocity changes, an azimuth thruster turning, or a propeller hitting ice. Furthermore, such excitations may take several different forms and are, in general, not stationary since their mean and auto-correlation vary between different finite time intervals [33].

For example, an azimuthing thruster turning corresponds to an excitation consisting mainly of low frequencies, while excitations by wave and sea loading have spectra containing harmonic frequency components multiples of the rotational speed [34], and classification societies suggest that excitations caused by propeller blade ice impacts could be modeled as a series of half-sines of varying amplitude [14,35]. A class of signal models that can capture the persistent and non-stationary characteristics of the unknown input signals is provided by the class of quasi-stationary signals [36].

Definition 1. A sequence $\{u(k)\}_{k\in\mathbb{N}}$ with $u(k) \in \mathbb{R}^m$ is said to be quasi stationary if

(i) The signal $u(k)$ is uniformly bounded, i.e.

$$\exists M \in \mathbb{R} : |u(k)| \le M \text{ all } k.$$

(ii) The auto-correlation sequence

$$R_u(h) = \lim_{N\to\infty} \frac{1}{2N} \sum_{k=-N}^{N} u(k)u^{\top}(k-h)$$

exists for all $h = 0, 1, \ldots$.

(iii) The signal $u(k)$ has bounded auto correlation

$$\sum_{h=-\infty}^{\infty} |R_u(h)| < \infty.$$

The cross-correlation function between two quasi-stationary signals $u(k)$ and $v(k)$, $k = 0, 1, \ldots$ is defined as

$$R_{u,v}(l,h) = \lim_{N\to\infty} \frac{1}{2N} \sum_{k=-N}^{N} u(k-l)v^{\top}(k-h)$$

and the cross-spectrum $\Phi_{u,v}(\omega)$ is given by

$$\Phi_s(\omega) = \begin{bmatrix} \Phi_{u,u}(\omega) & \Phi_{u,v}(\omega) \\ \Phi_{v,u}(\omega) & \Phi_{v,v}(\omega) \end{bmatrix}, \text{ for } s(k) = \begin{bmatrix} u(k) \\ v(k) \end{bmatrix}, \ k = 0, 1, \ldots .$$

Note that for a signal to be quasi-stationary, the auto-correlation function needs not be the same over all finite time intervals but merely exists in the limit. The assumption of uniform boundedness is not limiting in applications.

3.1. Power spectral density

In ship design and maneuvering, extensive work has been done on describing how fluctuations in wind and waves affects ships [37, Ch. 8]. For example, it is standard practice to model wind-induced forces in terms of their spectral densities, cf. [38] and the references therein. Hence, it is natural to also model torque excitations in a propulsion system in terms of their power spectral density. A quasi-stationary signal u has a rational power spectral density $\Phi_u(\omega)$ defined by the Fourier transform of $R_u(h)$ as

$$\Phi_u(\omega) = \sum_{h=-\infty}^{\infty} R_u(h)\mathrm{e}^{-\mathrm{i}h\omega}, \tag{9}$$

see e.g. [36,39,40].

An important and useful class of quasi-stationary signals are those with a rational power spectrum

$$\Phi_u(\omega) = W(\mathrm{e}^{\mathrm{i}\omega})W(\mathrm{e}^{-\mathrm{i}\omega}), \tag{10}$$

where $W(\mathrm{e}^{\mathrm{i}\omega})$ is a rational transfer function in $\mathrm{e}^{\mathrm{i}\omega}$, and is a spectral factor of $\Phi_u(\omega)$. A signal with rational spectral density $\Phi_u(\omega)$ can be realized as

$$u(k) = W(q^{-1})e(k) \tag{11}$$

where q^{-1} is the backwards-shift operator $q^{-1} : q^{-1}u(k) = u(k-1)$ and $e(k)$ is a quasi-stationary with constant spectrum. The transfer function $W(q^{-1})$ has poles inside the unit circle and zeros inside or on the unit circle, and $e(k)$ is a signal with constant spectrum (cf. the spectral factorization theorem [40,41]). Spectral factorization of a general positive rational function $\Phi_u(\omega)$ can for example be performed by Kalman-filtering techniques [41].

3.2. Proposed input model

Since different types of excitations may affect the system within any given time frame, an input-and-state observer should be robust with respect to all excitations which may affect the system. Although research on modeling ice-load excitations in propellers have been made [8,10–13], propeller ice-load interactions are still not fully understood.

Since a characterization in terms of spectral densities is, to the best knowledge of the authors, not readily available in the existing literature, it is not realistic to base the observer design on the nominal spectral density $\Phi_u(\omega)$. In order to guarantee a given performance in all situations, we introduce an upper bound $\bar{\Phi}(\omega)$, such that

$$\Phi_u(\omega) \leq \bar{\Phi}(\omega), \text{ for all } \omega \in [0,\ 2\pi). \tag{12}$$

In this study, we propose a simple but flexible spectral bound $\bar{\Phi}(\omega)$ that is capable of describing the following types of torque excitations affecting a marine propulsion system:

Type 1. A step-like change in input torque, caused by, for example, a sudden change in angular velocity.
Type 2. An excitation with spectrum bounded by a constant spectral density.
Type 3. Harmonic oscillations are caused by, for example, wave loading.
Type 4. Ice-load excitations.

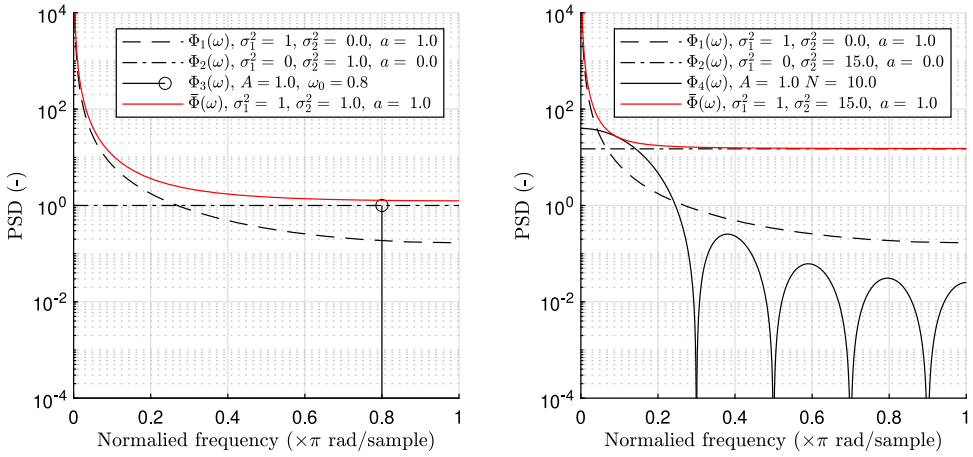

Fig. 2. Power spectral density (PSD) for various input models. The PSD $\Phi_1(\omega)$ corresponds to a random-walk model (13); $\Phi_2(\omega)$ corresponds to a constant spectral density (14); $\Phi_3(\omega)$ is the PSD of a harmonic oscillation with $\omega_{\max} = 0.8$ and amplitude $A_{\max} = 1$, $\Phi_4(\omega)$ is the PSD of an ice-load excitation modeled as in (17); and $\bar{\Phi}(\omega)$ is a spectral bound constructed from $\Phi_1(\omega)$ and $\Phi_2(\omega)$ as in (19). The figure illustrates how, by changing the parameters a, σ_1^2 and σ_2^2, $\bar{\Phi}(\omega)$ can provide an upper bound for a wide-range of input excitations.

An excitation of Type-1 consisting of a sequence of irregularly occurring steps with varying magnitudes and can be realized as

$$u_1(k) = au_1(k-1) + e_1(k), \tag{13}$$

where $e_1(k)$ is a quasi-stationary signal with constant spectral density $R_{e_1}(\omega) = \sigma_1^2$, has transfer function

$$W_1(\mathrm{e}^{-\mathrm{i}\omega}) = \frac{1}{1 - a\mathrm{e}^{-\mathrm{i}\omega}}, \quad a \in (0,\ 1],$$

and spectral density

$$\Phi_{u_1}(\omega) = W_1(\mathrm{e}^{\mathrm{i}\omega})\Phi_{e_1}(\omega)W_1(\mathrm{e}^{-\mathrm{i}\omega}) = \frac{1}{1 - 2a\cos(\omega) + a^2}\sigma_1^2.$$

For $a = 1$, (13) is referred to as a random-walk model and has been used for input estimation in [15,24,25,27,42]. A random-walk model has an infinite spectrum at frequency $\omega = 0$, which means that the signal is slowly diverging and has an infinite variance. Note that the random-walk model is not well suited for modeling excitations of Type 2–4 since it cannot capture high-frequency components of signals. This is a limitation since excitations affecting propulsion systems often contain harmonic oscillations of frequency multiples of the rotational speed.

The limiting case when $a = 0$ in (13) gives a signal with constant spectrum, which can be realized as

$$u_2(k) = e_2(k), \tag{14}$$

where $e_2(k)$ is a quasi-stationary signal with constant spectral density $R_{e_2}(\omega) = \sigma_2^2$ and has constant spectral density $\Phi_{e_2}(\omega) = \sigma_2^2$. Input-and-state estimation with input model (14) has for example been studied in [23]. Input model (14) represents the Type-2 excitation. Note that $u_2(k)$ cannot be used to model Type-1 excitations since it has zero mean.

Another important quasi-stationary signal is sinusoidal. A sinusoidal with normalized frequency f and amplitude A can be generated as

$$u(k) = 2\cos(2\pi f)u(k-1) - u(k-2) + A\delta(k), \tag{15}$$

where $\delta(k)$ is a single pulse of magnitude one at time instance $k = 0$. A torque excitation caused by a propeller blade hitting the ice was suggested in [13,14] to be modeled as a series of half-sines with varying magnitudes. In analogy with (15), a half-sine of length N (corresponds to normalized frequency $f = 1/(2N)$) and amplitude A is described by

$$u(k) = 2\cos(2\pi f)u(k-1) - u(k-2) + A\sin(2\pi f)(\delta(k) + \delta(k-N)) \tag{16}$$

with $\delta(k)$ a unit pulse at time k. Applying the filter

$$W_4(\mathrm{e}^{-\mathrm{i}\omega}) = \frac{A\sin(2\pi f)(1 + \mathrm{e}^{-N\mathrm{i}\omega})}{1 - 2\cos(2\pi f)\mathrm{e}^{-\mathrm{i}\omega} + \mathrm{e}^{-2\mathrm{i}\omega}}, \tag{17}$$

to a pulse sequence $\{e(k)\}$ generates a quasi-stationary signal consisting of irregularly spaces half-sines of length N. A limitation of the input model (16) is that for the sampling rates used, an excessively high-order filter W_4 may be required to describe the disturbances.

In practice, the characteristics of the input load can vary considerably between different time instants. Although adaptive methods could be applied, attempting to model the input characteristics accurately is seldom realistic, or it may lead to models which are overly complicated or of a high order, such as the half-sine wave model in (16). Instead, a more practical approach is to use a simple model whose spectrum over-bounds the signal spectra. As shown in Section 4, over-bounding the true signal spectrum would guarantee a given performance level for the input estimation. A simple signal model which provides convenient upper bounds for signals which typically occur in practice can be constructed as a combination of the signals (13) and (14), i.e.,

$$u(k) = u_1(k) + u_2(k). \tag{18}$$

The combined signal has spectral density

$$\Phi_u(\omega) = W(\mathrm{e}^{\mathrm{i}\omega})W(\mathrm{e}^{-\mathrm{i}\omega}) = \frac{1 + 2c\cos(\omega) + c^2}{1 - 2a\cos(\omega) + a^2}\sigma_e^2 \tag{19}$$

and spectral factor

$$W(\mathrm{e}^{\mathrm{i}\omega}) = \frac{1 + c\mathrm{e}^{-\mathrm{i}\omega}}{1 - a\mathrm{e}^{-\mathrm{i}\omega}}\sigma_e \tag{20}$$

where

$$c = \frac{r_0}{2r_1} + \sqrt{\left(\frac{r_0}{2r_1}\right)^2 - 1}, \quad \sigma_e^2 = \frac{r_1}{c},$$

and $r_0 = (1 + a^2)\sigma_2^2 + \sigma_1^2, \quad r_1 = -a\sigma_2^2$, see Appendix B. Note that multiplying $W(\mathrm{e}^{\mathrm{i}\omega})$ with $\mathrm{e}^{\mathrm{i}\omega}$ does not change the spectral density, and a signal $u(k)$ with spectra $\Phi_u(\omega)$ can be modeled as

$$u(k) = au(k-1) + e(k-1) + ce(k-2), \tag{21}$$

where $e(k)$ is a scalar quasi-stationary signal with constant spectral density.

The two components of the simple signal model (18) can be selected to over-bound different input spectra. This is illustrated in Fig. 2, which depicts the power spectral density of (18) for various values of the design parameters a, σ_1^2 and σ_2^2. Here, the first signal component u_1 provide a bound at low frequencies, while the second component u_2 can be selected to achieve the required bound at higher frequencies. This way, proper spectral bounds are obtained at low and high frequencies. Parameters a, σ_1 and σ_2 are considered application-specific design parameters that should be tuned to provide an appropriate spectral bound.

4. Simultaneous input and state estimation

The problem of designing a time-invariant input-and-state observer for system (7)–(8), which guarantees a given performance for all inputs with spectra bounded by (12), can now be formulated as the following worst-case estimation problem.

Problem. Find a stable filter $\hat{z} = \mathcal{F}y$ for the system (7)–(8) which minimizes the worst-case average cost

$$\bar{J}(\mathcal{F}) = \sup_u\{\|z - \hat{z}\|_{\mathcal{P}}^2 : \Phi_u(\omega) \le \bar{\Phi}(\omega) \text{ for all } \omega\} \tag{22}$$

where the squared power semi-norm is defined as

$$\|z - \hat{z}\|_{\mathcal{P}}^2 = \frac{1}{2\pi}\int_0^{2\pi} \mathrm{tr}(\Phi_{z-\hat{z}}(\omega))\mathrm{d}\omega = \mathrm{tr}(R_{z-\hat{z}}(0)).$$

As the spectral density $\Phi_{z-\hat{z}}(\omega)$ is a monotonically increasing function of $\Phi_u(\omega)$ for all $\mathcal{F}$ it follows that the solution of the worst-case problem defined by (22) is equivalent to minimizing the quadratic cost

$$J_z(\mathcal{F}) = \|z - \hat{z}\|_{\mathcal{P}}^2$$

for the system (7)–(8) with input $u = \bar{u}$ having spectrum $\Phi_u(\omega) = \bar{\Phi}(\omega)$.

The quadratic cost $J_z(\mathcal{F})$ can be minimized using a Kalman filter. For this purpose, we need a state–space model of the extended system from inputs v, e to outputs y, z. For convenience, a time delay can be introduced to the filter W from e to $u = We$, where $W(\mathrm{e}^{\mathrm{i}\omega})$ is a spectral factor of $\bar{\Phi}(\omega)$, and W can be assumed to have a state–space representation $W(q) = C_{\mathrm{W}}(qI - A_{\mathrm{W}})^{-1}B_{\mathrm{W}}$. This does not affect the input spectrum, and implies therefore no restriction. A minimal state–space realizations of (20), where a time-delay has been introduced to eliminate the direct feedthrough from e to u, is for example given by

$$A_{\mathrm{W}} = \begin{bmatrix} a & c \\ 0 & 0 \end{bmatrix}, B_{\mathrm{W}} = \begin{bmatrix} 1 \\ 1 \end{bmatrix}, C_{\mathrm{W}} = \begin{bmatrix} 1 & 0 \end{bmatrix}.$$

Augmenting (7)–(8) with (11) gives the augmented state–space system

$$x_{\mathrm{e}}(k+1) = A_{\mathrm{e}}x_{\mathrm{e}}(k) + F_{\mathrm{e}}v_{\mathrm{e}}(k), \tag{23}$$

$$y(k) = C_{\mathrm{e}}x_{\mathrm{e}}(k) + D_{\mathrm{e}}v_{\mathrm{e}}(k), \tag{24}$$

$$z(k) = T_{\mathrm{e}}x_{\mathrm{e}}(k), \tag{25}$$

with extended state and noise vectors

$$x_{\mathrm{e}}(k) = \begin{bmatrix} x_{\mathrm{W}}(k) \\ x(k) \end{bmatrix}, \; v_{\mathrm{e}}(k) = \begin{bmatrix} e(k) \\ v(k) \end{bmatrix},$$

and system matrices

$$A_{\mathrm{e}} = \begin{bmatrix} A_{\mathrm{W}} & 0 \\ BC_{\mathrm{W}} & A \end{bmatrix}, \; F_{\mathrm{e}} = \begin{bmatrix} B_{\mathrm{W}} & 0 \\ 0 & F \end{bmatrix}, \; C_{\mathrm{e}} = \begin{bmatrix} 0 & C \end{bmatrix}, \; D_{\mathrm{e}} = \begin{bmatrix} 0 & D \end{bmatrix}. \tag{26}$$

The vector $z(k)$, which is to be estimated, is a linear combination of the states $x_{\mathrm{e}}(k)$ and given by (cf. (8))

$$z(k) = T_{\mathrm{e}} x_{\mathrm{e}}(k) = \begin{bmatrix} u(k-1) \\ Tx(k) \end{bmatrix}. \tag{27}$$

Assuming that the estimator $\hat{z} = \mathcal{F} y$ at time instant k has access to the measured outputs $y(k), y(k-1), y(k-2), \ldots$ it is important to specify the instant $k+h$ at which a signal $z(k+h)$ is estimated. Denoting the optimal estimate of $z(k+h)$ based on $y(k), y(k-1), y(k-2), \ldots$ by $\hat{z}(k+h|k)$, it is obvious that

$$\hat{z}(k+h|k) = T_{\mathrm{e}} \hat{x}_{\mathrm{e}}(k+h|k)$$

where $\hat{x}_{\mathrm{e}}(k+h|k)$ is the optimal state estimate minimizing the quadratic cost

$$J_{x_{\mathrm{e}}}(\mathcal{F}) = \|x_{\mathrm{e}} - \hat{x}_{\mathrm{e}}\|_p^2.$$

The optimal state estimate can be computed using an augmented Kalman filter. Although one could use the system model (23) to predict future states $x(k+h)$ and inputs $u(k+h)$ for $h > 0$, we are here interested in collecting accurate estimates with no need to predict future values. Therefore, we will focus on finding the filtering estimate $\hat{z}(k|k)$ and smoothed estimate $\hat{z}(k-L|k)$ for $L > 0$. In the Kalman filter approach, these are found by first computing the optimal predictive state estimate $\hat{x}_{\mathrm{e}}(k+1|k)$, followed by a sequential computation of $\hat{z}(k|k), \hat{z}(k-1|k), \ldots$. The notation

$$P_0 = \lim_{N\to\infty} \frac{1}{2N} \sum_{k=-N}^{N} (x(k+1) - \hat{x}(k+1|k))(x(k+1) - \hat{x}(k+1|k))^{\top},$$

will be used.

The predictive estimate for x_{e} is given by the standard Kalman filter

$$\hat{x}_{\mathrm{e}}(k+1|k) = A_{\mathrm{e}} \hat{x}_{\mathrm{e}}(k|k-1) + K_0 (y(k) - C_{\mathrm{e}} \hat{x}_{\mathrm{e}}(k|k-1)) \tag{28}$$

where

$$K_0 = A_{\mathrm{e}} P_0 C_{\mathrm{e}}^{\top} \left(C_{\mathrm{e}} P_0 C_{\mathrm{e}}^{\top} + D_{\mathrm{e}} D_{\mathrm{e}}^{\top} \right)^{-1} \tag{29}$$

is given by the discrete-time algebraic Riccati equation

$$P_0 = A_{\mathrm{e}} P_0 A_{\mathrm{e}}^{\top} - K_0 (C_{\mathrm{e}} P_0 C_{\mathrm{e}}^{\top} + D_{\mathrm{e}} D_{\mathrm{e}}^{\top}) K_0^{\top} + F_{\mathrm{e}} F_{\mathrm{e}}^{\top}. \tag{30}$$

Although the results are derived for systems where all input signals are unknown, extending the augmented Kalman-filtering framework to systems with known input signals is straightforward.

It is well known that estimates can be improved with fixed-lag smoothing [43,44], that is, $\hat{x}_{\mathrm{e}}(k+1-L|k)$ is estimated instead of $\hat{x}_{\mathrm{e}}(k+1|k)$. In this application, the number of states $x_{\mathrm{e}}(k)$ are typically much larger than elements in $z(k)$. To avoid a filter of unnecessarily high order, which may negatively impact the real-time performance, a signal smoother estimating $\hat{z}(k-L+1|k)$ is used instead of a full-state smoother. Augmenting (23)–(24) with delayed elements $z(k-1), z(k-2), \ldots, z(k-L-1)$ gives the extended system

$$x_{\mathrm{s}}(k+1) = A_{\mathrm{s}} x_{\mathrm{s}}(k) + F_{\mathrm{s}} v_{\mathrm{e}}(k), \quad y(k) = C_{\mathrm{s}} x_{\mathrm{s}}(k) + D_{\mathrm{e}} v_{\mathrm{e}}(k), \tag{31}$$

with

$$x_{\mathrm{s}}(k) = \begin{bmatrix} x_{\mathrm{e}}(k) \\ z(k-1) \\ z(k-2) \\ \vdots \\ z(k-L-1) \end{bmatrix}, \; A_{\mathrm{s}} = \begin{bmatrix} A_{\mathrm{e}} & 0 & \cdots & 0 & 0 \\ T_{\mathrm{e}} & 0 & \cdots & 0 & 0 \\ 0 & I & \cdots & 0 & 0 \\ \vdots & & \ddots & & \vdots \\ 0 & 0 & \cdots & I & 0 \end{bmatrix}, \; F_{\mathrm{s}} = \begin{bmatrix} F_{\mathrm{e}} \\ 0 \\ 0 \\ \vdots \\ 0 \end{bmatrix}, \; C_{\mathrm{s}} = \begin{bmatrix} C_{\mathrm{e}} & 0 & 0 & \cdots & 0 \end{bmatrix}.$$

The extended system can be used to synthesize an optimal fixed-lag signal smoother by Kalman-filtering techniques, cf. (28)–(30). The fixed-lag signal smoother is of the form

$$\hat{x}_{\mathrm{s}}(k+1|k) = A_{\mathrm{s}} \hat{x}_{\mathrm{s}}(k|k-1) + K_{\mathrm{s}} (y(k) - C_{\mathrm{s}} \hat{x}_{\mathrm{s}}(k|k-1)),$$

with $K_{\mathrm{s}} = \begin{bmatrix} K_0^{\top} & K_1^{\top} & \cdots & K_{L+1}^{\top} \end{bmatrix}^{\top}$. The Kalman gains K_i are either obtained by solving a Riccati equation as in (29)–(30) or computed recursively from K_0 and P_0, cf. [25,43,44].

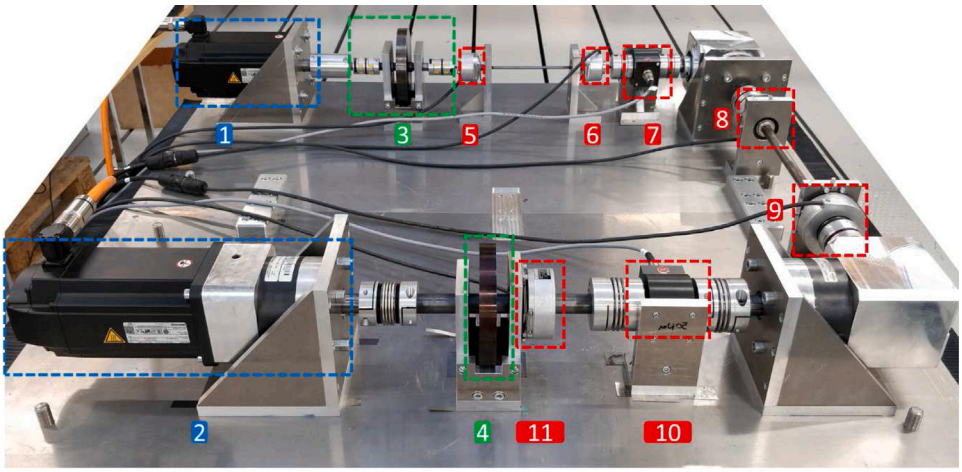

(a) The test bench.

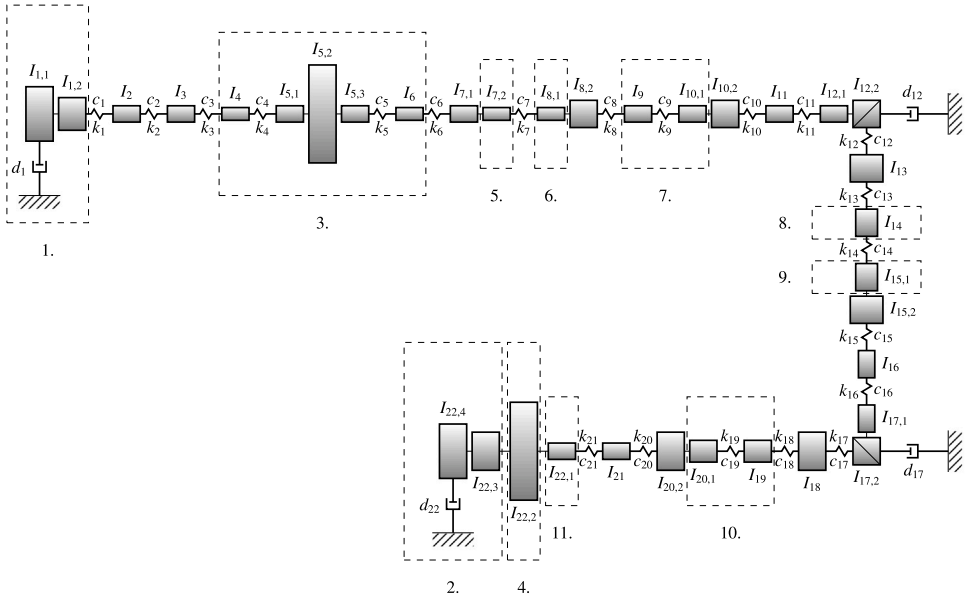

(b) Lumped-mass model.

Fig. 3. (a) Picture of the test bench. (b) A lumped-mass model of the test bench. The components of the test bench are: 1. Driving motor, 2. Load generator, 3. Flexible coupling, 4. Propeller mass, 5. and 6. ERN 420 hollow-through shaft rotary TTL encoders, 7. Torque transducer ±20 Nm 8. and 9. ERN 120 hollow-through shaft rotary TTL encoders. 10. Torque transducer ±50 Nm, 11. ERN 120 hollow-through shaft rotary TTL encoder.

5. Experiment: Laboratory-scale test bench

Experiments on a laboratory-scale test bench have been conducted to evaluate the performance of the proposed input and state estimator. The experiments were designed to emulate a thruster operated in ice-load conditions. Different input designs for the augmented Kalman filter presented in Section 4 are compared to a conventional approach where the dynamics of the drivetrain are ignored. The experiments demonstrate the importance of accounting for the dynamics of the system when estimating torque and illustrate how design choices affect the estimation results.

5.1. Experiment setup

A test bench was built to conduct a series of reference measurements. The test bench consisted of two synchronous servomotors, a flexible coupling, five hollow-through shaft rotary encoders, two torque transducers, three gears (with ratios of 1:3, 1:4, and

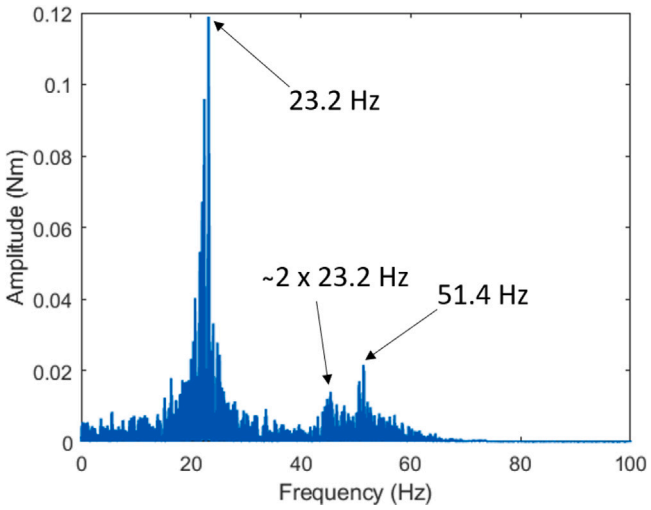

Fig. 4. Single-sided amplitude spectrum of the torque response at the input shaft during the PRBS experiment. The experiment reveals the natural frequencies of the system.

8:1), propeller mass, and several couplings and shafts. A picture of the test bench is presented in Fig. 3(a). The two servo motors (Bosch Rexroth MS2N06-D0BNN) had a nominal torque of 11.9 Nm and a maximum rotational frequency equal to 6000 rpm. One of these motors was used as a driving motor, and the other motor generated loads. The purpose of the loading motor was to generate excitations similar to those affecting a propeller in a marine propulsion system. A planetary gear with a gear ratio of 8:1 was installed on the loading motor to allow the use of a servo motor of the same size as on the driving side. With the load generator, excitations or load curves could be applied to the system.

The test bench was designed to have similar properties as the driveline of azimuth thrusters used in marine vessels. When scaling the dimensions of a full-size thruster to approximately one-thousandth, all the physical properties of the full-size driveline cannot be replicated. Hence, the goal with the test-bench design was not to replicate the dynamical behavior of any existing thruster but to have a laboratory-scale test setup with similar key features as a full-size thruster. The following three key features were taken into consideration in the design:

(i) The systems should have similar natural frequencies.
(ii) The angular displacement of shafts should be comparable at nominal load.
(iii) The nominal rotational velocity of the loading-motor shaft should be comparable to that of propeller shafts.

The choice to emphasize the two lowest natural frequencies is motivated by the fact that the large excitations occur typically at low frequencies. Such excitations include the first and second-order blade frequencies. Furthermore, in practical applications, the torsional response of a thruster driveline is typically dominated by frequencies below the system's first and second natural frequencies.

The flexible coupling in the driving motor shaft was constructed from two elastomer couplings with an added mass in between, such that the lowest torsional natural frequencies of the test bench are comparable to those of typical full-size drivetrains. By applying a pseudo-random binary sequence (PRBS) excitation to the load generator while rotating the test bench with a constant nominal velocity, the two most dominant resonance frequencies of the system were determined to be approximately 23.2 and 51.4 Hz. A single-sided amplitude spectrum of the torque response at the input shaft during the PRBS experiment is presented in Fig. 4. This can be compared with full-size azimuth thrusters, which typically have the lowest natural frequencies in the ranges 10–25 Hz and 20–40 Hz. The angular deflection at the driving motor side was approximately 2.9 degrees in normal operation conditions without excitations. The nominal velocity of the test bench was approximately 3200 rpm on the driving side and 267 rpm on the loading side.

Five Heidenhain hollow-through shaft rotary TTL encoders (three ERN 120 and two ERN 420) with 5000 pulses per revolution were used to measure the velocity of each shaft as well as the angular displacement of the shaft after the flexible coupling and between the first two gears. Encoder pulse data was converted into angles by counting pulses within a sampling interval which, in turn, was converted into angular velocity using finite difference approximation. Torque transducers (ETH-Messtechnik DRBK) were used to measure the torque before and after the angle gears, with torque ranges ±20 Nm and ±50 Nm, respectively.

Data acquisition and control were realized with a National Instrument CompactRIO (NI cRIO-9057). Each sensor was connected to a measurement module mounted to the CompactRIO, and Labwiew FPGA was used in the measurements. The encoders were connected to a digital measurement module NI 9411 and the torque transducers to an analog measurement module NI 9215. The test bench control software was running in Labview, and the CompactRIO communicated with the motor drives over EtherCAT. Motors could be operated in either torque or velocity control mode. Both motors were controlled with field-oriented control (FOC).

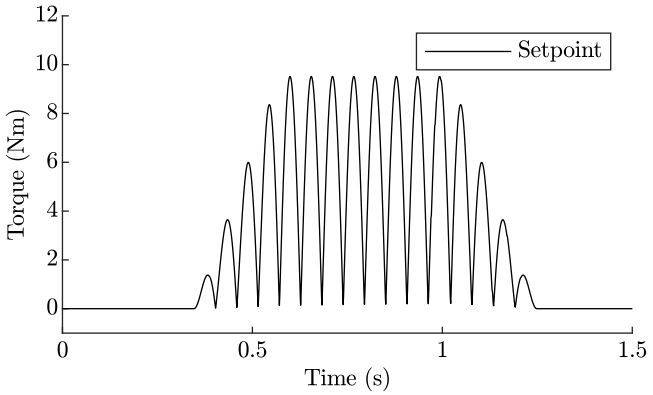

Fig. 5. Torque setpoint of the loading motor in the experiment.

Table 1
List of components and parameters used to model the experiment test bench.

Components	Index i	I_i (kgm^2)	c_i (Nm/(rad/s))	k_i (Nm/rad)	d_i (Nm/(rad/s))
Driving motor, coupling	1	7.94×10^{-4}	8.08	1.90×10^{5}	0.0030
Shaft	2	3.79×10^{-6}	0.29	6.95×10^{3}	0
Elastomer coupling hub	3	3.00×10^{-6}	0.24	90.00	0
Elastomer coupling middle piece	4	2.00×10^{-6}	0.24	90.00	0
Elastomer coupling hubs & shaft	5	7.81×10^{-3}	0.24	90.00	0
Elastomer coupling middle piece	6	2.00×10^{-6}	0.24	90.00	0
Elastomer coupling hub, encoder & shaft	7	3.17×10^{-6}	0.00	30.13	0
Shaft, encoder & coupling	8	5.01×10^{-5}	1.78	4.19×10^{4}	0
Torque transducer	9	6.50×10^{-6}	0.23	5.40×10^{3}	0
Torque transducer & coupling	10	5.65×10^{-5}	1.78	4.19×10^{4}	0
Shaft	11	4.27×10^{-6}	0.52	1.22×10^{3}	0
Shaft & gear	12	3.25×10^{-4}	1.84	4.33×10^{4}	0.0031
Coupling	13	1.20×10^{-4}	1.32	3.10×10^{4}	0
Shaft	14	1.15×10^{-5}	0.05	1.14×10^{3}	0
Shaft & coupling	15	1.32×10^{-4}	1.32	3.10×10^{4}	0
Shaft	16	4.27×10^{-6}	0.52	1.22×10^{4}	0
Shaft & gear	17	2.69×10^{-4}	1.88	4.43×10^{4}	0.0031
Coupling	18	1.80×10^{-4}	5.86	1.38×10^{5}	0
Torque transducer	19	2.00×10^{-5}	0.85	2.00×10^{4}	0
Torque transducer & coupling	20	2.00×10^{-4}	5.86	1.38×10^{5}	0
Shaft	21	4.27×10^{-6}	0.52	1.22×10^{4}	0
Shaft, mass & loading motor	22	4.95×10^{-2}	–	–	0.2400

The output torques of the motors were calculated in the motor drives from the phase currents. Thus, torque caused by, for example, absolute damping in motors was not measured directly.

5.2. Input excitations

The experiment was set up to mimic operation in ice-load conditions. The angular velocity of the driving motor was controlled to a constant nominal speed (3200 rpm) by varying the driving-motor torque. When the system was in a steady state, an excitation was applied by the loading motor. Input excitations were designed based on ice-load classes used by ship classification societies [14,35]. Ice hitting the propeller was modeled as a series of half sine waves with varying magnitudes. In Fig. 5 the torque excitation used in the experiments is presented. The excitation is representative of a four-blade propeller interacting with ice and was computed as in [13], with amplitudes scaled to be of suitable magnitudes for the test bench.

5.3. Test-bench model and filter design

The system was modeled as outlined in Section 2 and the resulting lumped-mass model is illustrated in Fig. 3(b). A list of components with their respective mass moment of inertia, torsional stiffness, and damping coefficients is presented in Table 1. The torsional stiffness (Nm/rad) of cylindrical shafts are given by $k_i = G_i J_i / L_i$, where G_i is the shear modulus (Pa) of the shaft, $J_i = \pi D_i^4/32$ (m^4) the torsional constant of a solid shaft, D_i the shaft diameter (m) and L_i the shaft length (m). It was assumed that the torque losses were mainly due to absolute damping caused by the motors and gears and are thus neglected for other components.

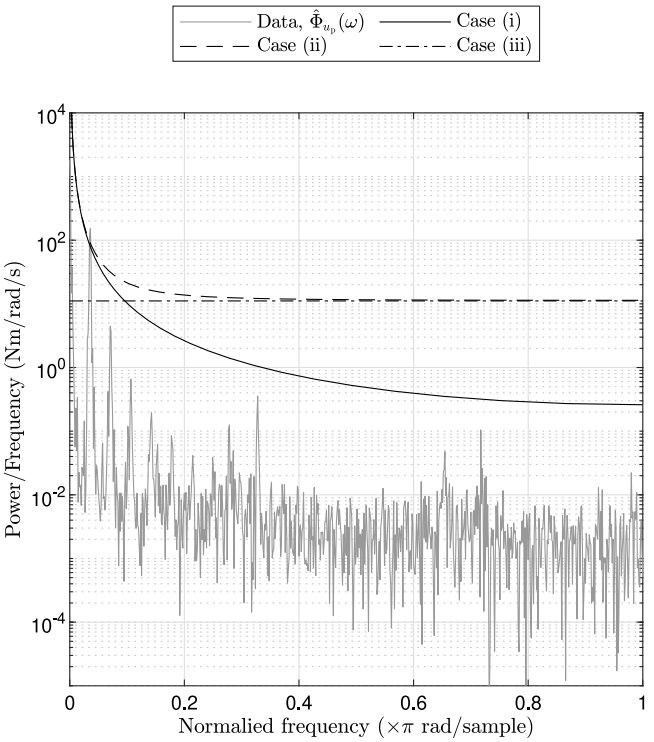

Fig. 6. Single-sided power spectra for design cases (i)–(iii) for the laboratory-scale test-bench experiments, and the estimated propeller-torque power spectral density $\hat{\Phi}_{u_p}(k)$ using the Fourier transform based on data from the laboratory test bench.

The absolute damping coefficients of the gears and motors $d_i,\ i \in \{1, 12, 17, 22\}$ were identified from experiment data. Since torque measurements from the shaft between the two gears were not available, it was impossible to determine the individual gear losses. Instead, the total torque loss from gears was computed, and it was assumed that $d_{12} = d_{17}$.

In marine propulsion systems, the average torque is often known in practice. Hence, in the test-bench experiment, the driving-motor torque excitation $u_{\mathrm{m}}(k)$ and loading-motor torque $u_{\mathrm{p}}(k)$ are modeled as

$$u_{\mathrm{m}}(k) = \mu_{\mathrm{m}}(k) + W_{\mathrm{m}}(q)e_{\mathrm{m}}(k),$$
$$u_{\mathrm{p}}(k) = \mu_{\mathrm{p}}(k) + W_{\mathrm{p}}(q)e_{\mathrm{p}}(k),$$

where $\mu_{\mathrm{m}} = 2.7$ Nm and $\mu_{\mathrm{p}}(k) = 0$ Nm are the known average input torques of the experiment, and $e_{\mathrm{m}}(k), e_{\mathrm{p}}(k)$ are quasi-stationary signals with constant spectra $\Phi_{e_{\mathrm{m}}}(\omega) = 1$ and $\Phi_{e_{\mathrm{p}}}(\omega) = 1$ for all ω. The transfer functions $W_{\mathrm{m}}(\mathrm{e}^{\mathrm{i}\omega})$ and $W_{\mathrm{p}}(\mathrm{e}^{\mathrm{i}\omega})$ were defined as in (20). In the experiment, the driving-motor torque varied in the interval $[\mu_{\mathrm{m}} - 2, \mu_{\mathrm{m}} + 2]$ Nm. Hence, by the three-sigma rule of thumb, $W_{\mathrm{m}}(q) = \sigma_{\mathrm{m}} = 2/3$ Nm was used to ensure robustness against (almost) all possible inputs. The input signal $u_{\mathrm{p}}(k)$ was assumed to have $\Phi_{u_{\mathrm{p}}} \leq \bar{\Phi}(\omega)$, $\omega \in [0,\ 2\pi)$, where $\bar{\Phi}(\omega)$ has a spectral factor W_{p} as proposed in Section 4. The largest allowed magnitude of excitation in the experiment was 10 Nm. Hence, the following design cases for the loading-motor torque were considered, where $W_{\mathrm{p}}(\mathrm{e}^{\mathrm{i}\omega})$ was given by (20) with parameters

(i) $a = 1,\ \sigma_1^2 = 1,\ \sigma_2^2 = 0.1,$
(ii) $a = 1,\ \sigma_1^2 = 1,\ \sigma_2^2 = (10/3)^2,$
(iii) $a = 0,\ \sigma_1^2 = 0,\ \sigma_2^2 = (10/3)^2.$

Input spectra for design cases (i)–(iii) are illustrated in Fig. 6. The power spectral density of the propeller torque excitation was estimated from data using the Fourier transform and is given in Fig. 6 as a reference. Design case (i) was based on data measured from the testbench and was included to illustrate the performance when $\bar{\Phi}(\omega)$ closely approximates the spectra of the true signal. Design cases (ii) and (iii) are robust against (almost) all possible input excitations, whereas case (ii) has unbounded spectra at $\omega = 0$ and can hence describe slowly diverging quasi-stationary signals.

Input and state estimators were synthesized based on the lumped-mass model presented in Fig. 3 for design cases (i)–(iii). Angular speed measurements $\dot{\theta}_7(k), \dot{\theta}_8(k)$ and torque measurement $\tau_9(k)$ from the driving-motor shaft were used in the estimation. The covariance matrix of the measurement noise was determined from experiments by analyzing the power spectra of the measured signals when rotating the driving motor at the constant angular velocity 338 rad/s and had the numerical value

Table 2
Worst-case estimation errors $P_{u_m-\hat{u}_m} = \|u_m - \hat{u}_m\|_P^2$ and $P_{u_p-\hat{u}_p} = \|u_p - \hat{u}_p\|_P^2$ for the laboratory-scale test-bench experiments using design cases (i)–(iii) with various fixed-lags L.

	$L=1$		$L=2$		$L=4$		$L=8$		$L=10$	
	$P_{u_m-\hat{u}_m}$	$P_{u_p-\hat{u}_p}$	$P_{u_m-\hat{u}_m}$	$P_{u_p-\hat{u}_p}$	$P_{u_m-\hat{u}_m}$	$P_{u_p-\hat{u}_p}$	$P_{u_m-\hat{u}_m}$	$P_{u_p-\hat{u}_p}$	$P_{u_m-\hat{u}_m}$	$P_{u_p-\hat{u}_p}$
(i)	0.44	7.91	0.44	6.91	0.44	5.07	0.42	3.43	0.42	3.22
(ii)	0.44	19.76	0.44	18.41	0.44	14.24	0.42	12.51	0.42	12.41
(iii)	0.44	11.11	0.44	11.08	0.44	10.38	0.42	10.22	0.42	10.19

Table 3
Worst-case estimation errors $P_{\tau_{19}-\hat{\tau}_{19}} = \|\tau_{19} - \hat{\tau}_{19}\|_P^2$ for the laboratory-scale test-bench experiments using design cases (i)–(iii) with various fixed-lags L.

	$L=1$	$L=2$	$L=4$	$L=8$	$L=10$
(i)	1.46	0.94	0.83	0.75	0.72
(ii)	1.53	0.95	0.85	0.76	0.74
(iii)	1.15	0.78	0.71	0.60	0.58

Table 4
Root-mean-square error (RMSE) of torque estimates in the laboratory test-bench experiments. Estimates for the AKF design-cases (i)–(iii) with fixed-lag $L = 10$ are compared to the case where dynamics of the system have been ignored.

	AKF (i)	AKF (ii)	AKF (iii)	Dynamics ignored
Driving motor torque (Nm)	0.47	0.47	0.49	–
Loading motor torque (Nm)	0.86	1.12	3.28	–
Torque response on the loading-motor shaft (Nm)	0.69	0.69	1.86	6.55

$R = \mathrm{diag}(0.05, 0.10, 0.20)$. The first two measurements are from encoders 1 and 2, respectively, and the third measurement is from torque transducer 1. All measured signals were low-pass filtered using the passband 500 Hz and down-sampled to a constant 1 kHz sampling rate.

Process noise $v_x(k)$ was modeled as white-noise with covariance matrix $Q = 0.01I$. The matrix F in (7) was defined such that process noise affects only states corresponding with angular velocities. The low process noise variance reflects the prior understanding that the system was well-balanced and that no external excitations act on gears, bearings, shafts, or couplings.

In Tables 2 and 3 worst-case estimation errors are presented for fixed-lag signal smoothers for various lags L. These errors are not based on experiments but on the specified noise covariances and input spectra used to design the filters. Since design case (ii) characterizes a larger class of excitations than design case (iii), worst-case estimation errors in (ii) are larger. However, as seen in Tables 2 and 3, smoothing can make the difference small. Since the worst-case errors can be conservative, experiments on the testbench were performed to evaluate the expected performance of the estimators. Results are presented in Section 5.4.

5.4. Results

Design cases (i)–(iii) from the previous section with fixed lag $L = 10$ were used for torque estimation in the test-bench experiments. The AKF-estimates were compared to estimates obtained by assuming that shafts are rigid, i.e., dynamics were ignored. Estimation results are compared against the measured input torques, as well as against the torque $\tau_{19}(k)$ measured at the driving motor shaft. Root-mean-square errors (RMSE) of torque estimates are presented in Table 4. The estimated input torques and torque responses are presented in Figs. 7 and 8 for design case (i) which resulted in the smallest estimation errors. Observe that input torque measurements are computed from the applied phase-current, while the real torque might also contain other excitations caused by, e.g., friction and imbalance in the system being measured. Based on these experiments, it was clear that the AKF-methods outperform the simple estimator that ignores the dynamics of the system. The RMSE of the AKF-methods coincides well with the derived worst-case errors presented in Tables 2 and 3. The fact that some estimation errors are larger than the theoretical bounds can be attributed to a mismatch between model and reality or transmission errors in gears. When comparing results obtained with AKF-method with estimates where the dynamics were ignored, the importance of properly accounting for the system's dynamics becomes evident.

6. Experiment: Sea trial

Results from a preliminary full-scale test are presented based on measurements from an underwater-mountable azimuth thruster, cf. Fig. 1. The maximum rotational speed of the input shaft is 750 rpm, and the nominal input torque of the thruster is 70 kNm. The experiment was conducted at close to the constant rotational speed of 630 rpm. The azimuth-thruster drivetrain was modeled as in Section 2, the gear ratio of the system is $n = 13/62$, and torque losses in gears are approximated to be 3% of the transmitted torque. Stiffness and damping parameters of shafts were computed based on the specified shear-modulus and dimensionless damping factors of the shaft materials.

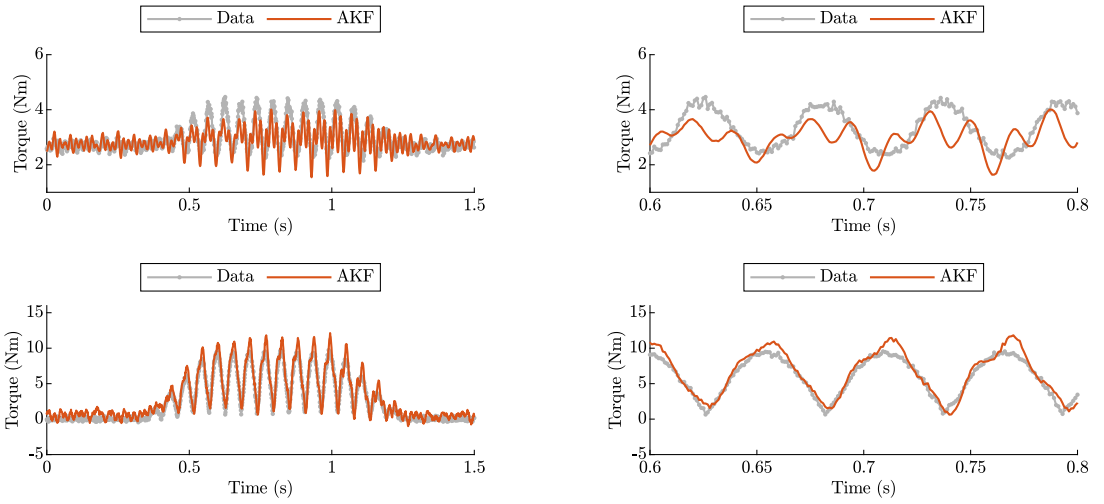

(a) Driving motor torque (top) and loading motor torque (bottom).

(b) Driving motor torque (top) and loading motor torque (bottom). Zoomed-in at 0.6-0.8s.

Fig. 7. Measured and estimated input torques for the laboratory test bench experiments using the augmented Kalman filter with input model (i).

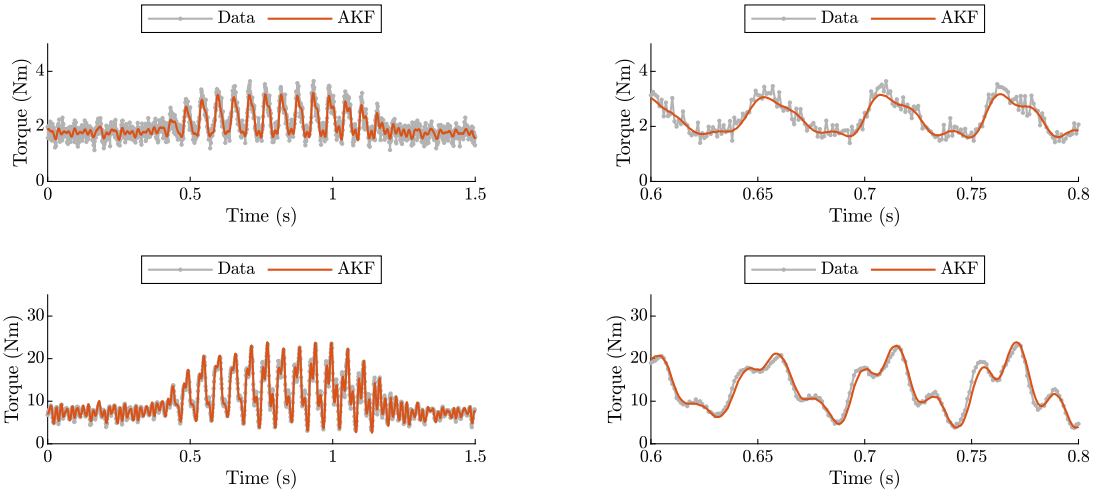

(a) Torque response at the driving-motor shaft (top) and loading-motor shaft (bottom).

(b) Torque response at the driving-motor (top) and loading-motor shaft (bottom). Zoomed-in at 0.6-0.8s.

Fig. 8. Measured and estimated torques responses at the driving-motor shaft ($i = 9$) and loading-motor shaft ($i = 19$) in the laboratory test bench experiment. Torques were estimated using the augmented Kalman filter with input model (i).

The input shaft of the thruster drivetrain was instrumented with a Metapower® torque and angular velocity monitoring system [45]. A strain gauge used for validation purposes was installed at the propeller shaft. However, reliability issues with the strain gauge resulted in inaccurate measurements. The measured signal contained spurious large-amplitude harmonic oscillations which were removed by data post-processing before the estimation step.

A few possible sources for the measurement errors are that the strain gauge was not correctly compensating for bending in the shaft, the sensor was malfunctioning, or installed incorrectly. Furthermore, due to the inconvenient location of the sensor, performing maintenance on it is was impossible. This further shows the importance of developing reliable estimation methods that rely only on inboard measurements. Although the encountered sensor problems limit the conclusions that can be drawn from the experiment, the sea trial still demonstrates that the technologies applied in laboratory-scale tests can be successfully implemented on full-size systems.

Table 5
Worst-case estimation errors for input torques ((kNm)^2) and torque responses at various locations on the drivetrain in the sea trial are presented.

Location	$\|z_i - \hat{z}_i\|_p^2$
Motor shaft	0.0143
Flexible coupling	0.0102
Metapower	0.0074
Gear coupling	0.0083
Gear	0.0088
Propeller shaft	0.5614
Motor input torque	1.0777
Propeller input torque	9.0521

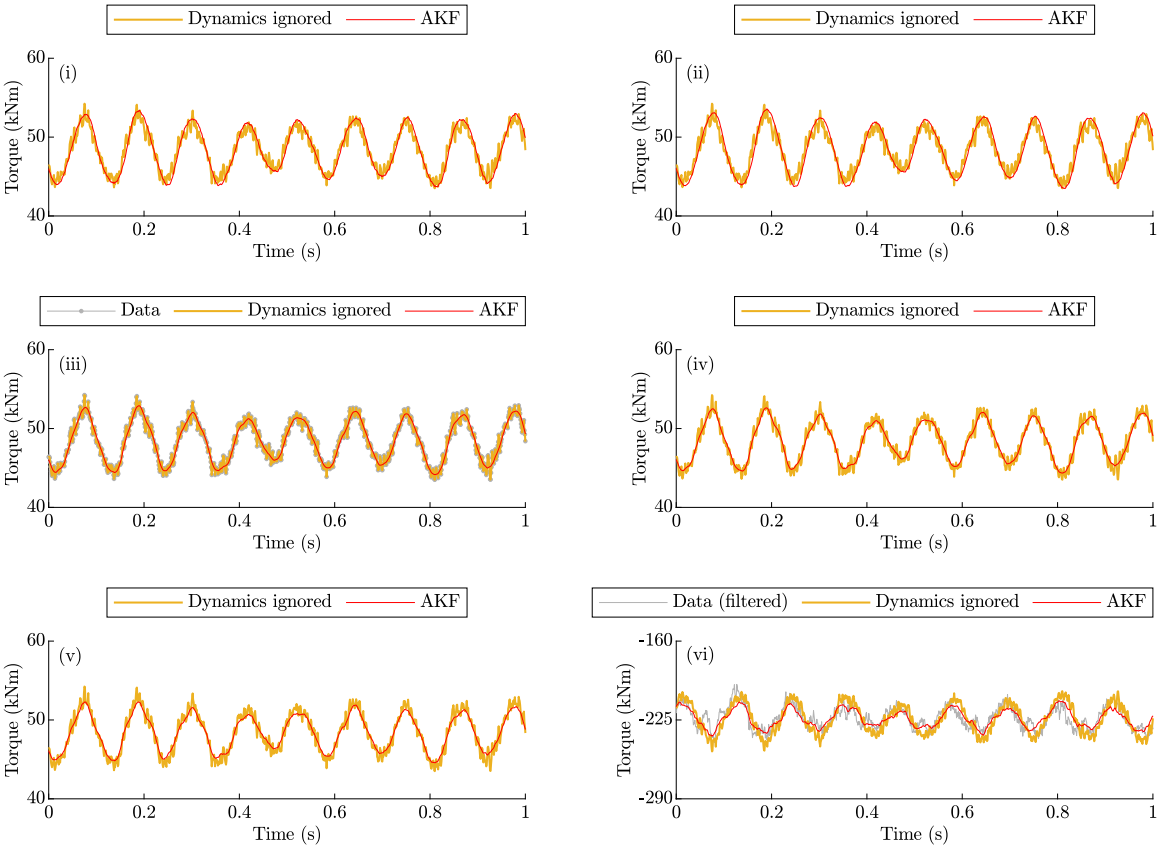

Fig. 9. Estimated torque responses at the (i) motor shaft, (ii) flexible coupling, (iii) Metapower, (iv) gear coupling, (v) gear, (vi) propeller shaft of a full-size azimuth thruster.

Spectral bound $\bar{\Phi}(\omega)$ on the unknown input torques was designed as outlined in Section 3.1 with parameters $a = 1$, $\sigma_1 = 1000$ and $\sigma_2^2 = 0$, such that

$$u_{\mathrm{m}}(k) = nW(q^{-1})e_{\mathrm{m}}(k),$$
$$u_{\mathrm{p}}(k) = W(q^{-1})e_{\mathrm{p}}(k).$$

The fixed-lag $L = 10$ was used when designing the signal smoother. Angular speed measurements were assumed to have noise covariance 0.001 (rad/s) and torque measurements to have covariance 10^6 (Nm). The covariance of process noise affecting angular velocities $\dot{\theta}_i(k)$ between the motor and the gear were set to 0.010 (rad/s) and 0.003 (rad/s) for the propeller shaft. Process noise covariance affecting states $\Delta\theta_i(k)$ were set to zero. The resulting worst-case error are given in Table 5 and estimation results are presented in Figs. 9 and 10. The augmented Kalman filter and the case where shaft dynamics were ignored yielded similar results in this case study. This is because the system is operating in normal operating conditions without large excitations, in which circumstances the shaft flexibility has only a limited effect on its behavior. In practice, the actual benefits of the proposed methods are mainly in dynamic transient conditions.

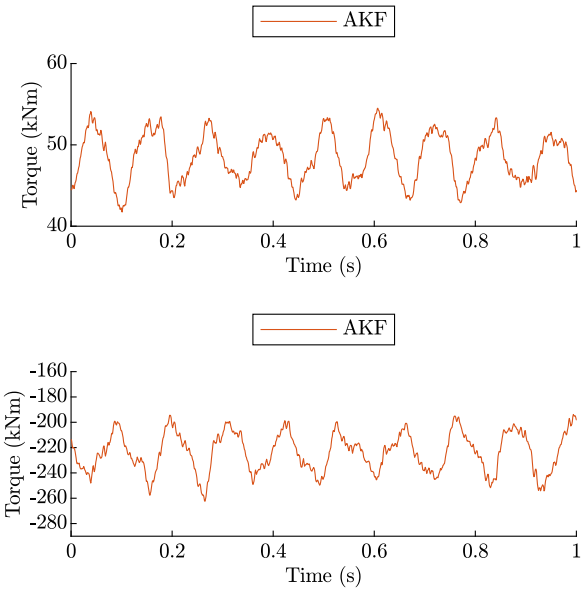

Fig. 10. Estimated motor torque (top) and propeller torque (bottom) of a full-size azimuth thruster using the proposed augmented Kalman filter.

7. Conclusions

The focus of this paper has been on the design of observers for torque estimation in a marine propulsion system. In contrast to other state-of-the-art SISE algorithms, where unknown input signals are assumed to be completely unknown, we have described input excitations as quasi-stationary signals with bounded power spectral density. It is shown that, given a spectral bound of the unknown inputs, a worst-case optimal linear time-invariant observer can be synthesized as an augmented Kalman filter. The performance of the proposed input-and-state observer has been validated in a laboratory-scale test-bench with similar properties to a full-scale marine propulsion system operating in ice-load conditions. Experiments demonstrate the importance of accounting for dynamics when estimating torque responses. The presented results show that torque estimates can be obtained based on a few indirect measurements at convenient locations on the driving motor shaft and have accuracy comparable to direct measurements using, e.g., strain gauges. The proposed input-and-state observer has been implemented on a full-size underwater mountable azimuthing thruster, and estimation results have been presented.

With the results from this study, it can be concluded that unknown input torque excitations and torque responses at all locations on the drivetrain can be estimated with high accuracy based on a few measurements taken from a convenient location on the motor shaft. By collecting torque data using the proposed technology, we expect that the nature of torque excitations, such as propeller-ice interactions and their effect on components remaining useful lifetime, can be better understood in the future.

CRediT authorship contribution statement

Mikael Manngård: Conceptualization, Methodology, Software, Validation, Formal analysis, Writing – original draft, Writing – review & editing, Visualization. **Ivar Koene:** Methodology, Validation, Investigation, Writing – review & editing. **Wictor Lund:** Software. **Sampo Haikonen:** Methodology, Validation, Investigation, Writing – review & editing. **Fredrik A. Fagerholm:** Supervision. **Michał Wilczek:** Supervision. **Konrad Mnich:** Supervision. **Joni Keski-Rahkonen:** Methodology, Supervision, Writing – review & editing, Project administration. **Raine Viitala:** Supervision, Project administration. **Jerker Björkqvist:** Supervision, Project administration. **Hannu T. Toivonen:** Conceptualization, Methodology, Supervision, Writing – review & editing.

Declaration of competing interest

The authors declare that they have no known competing financial interests or personal relationships that could have appeared to influence the work reported in this paper.

Acknowledgments

This work was done within the Business Finland funded research project Reboot IoT Factory. The authors would like to thank the anonymous reviewers for their meticulous reviews and constructive comments, which were of great help to improve the manuscript.

Appendix A

The system matrices A_c and B_c of the continuous-time model (5) have the following form:

$$A_c = \left[\begin{array}{c|c} A_{11} & A_{12} \\ \hline A_{23} & 0 \end{array}\right]$$

$$= \left[\begin{array}{ccccc|ccc} -\frac{(c_1 n_1^2 + d_1)}{I_1} & \frac{c_1 n_1}{I_1} & 0 & & & -\frac{k_1}{I_1} & & \\ \frac{c_1 n_1}{I_2} & -\frac{(c_1 + c_2 n_2^2 + d_2)}{I_2} & \frac{c_2 n_2}{I_2} & & & \frac{k_1}{I_2} & -\frac{k_2}{I_2} & \\ & \ddots & \ddots & \ddots & & & \ddots & \ddots \\ & & \frac{c_{N-2} n_{N-2}}{I_{n-1}} & -\frac{(c_{N-2} + c_{N-1} n_{N-1}^2 + d_{N-1})}{I_{N-1}} & \frac{c_{N-1} n_{N-1}}{I_{N-1}} & & \frac{k_{n-2}}{I_{N-1}} & \frac{k_{N-1}}{I_{N-1}} \\ & & 0 & \frac{c_{N-1} n_{N-1}}{I_N} & -\frac{(c_{N-1} + d_N)}{I_N} & & & \frac{k_{N-1}}{I_N} \\ \hline & & n_1 & -1 & & 0 & \cdots & 0 \\ & & & \ddots & \ddots & \vdots & \ddots & \vdots \\ & & & & n_{N-1} \quad -1 & 0 & \cdots & 0 \end{array}\right],$$

$$B_c = \left[\begin{array}{c} B_1 \\ \hline 0 \end{array}\right] = \left[\begin{array}{cc} \frac{1}{I_1} & 0 \\ 0 & 0 \\ \vdots & \vdots \\ 0 & -\frac{1}{I_N} \\ \hline 0 & 0 \end{array}\right],$$

where zero elements have been left out.

Appendix B

From (13), (14), and (18)

$$\begin{aligned} u(k) - au(k-1) &= u_1(k) + u_2(k) - au_1(k-1) - au_2(k-1) \\ &= e_1(k) + e_2(k) - ae_2(k-1). \end{aligned}$$

To find a spectral factor of $u(k)$, a realization in terms of a single scalar white-noise variable $e(k)$ with variance σ_e^2 is to be found. By the simple structure of the model, such an realization should be of the form

$$\tilde{u}(k) - a\tilde{u}(k-1) = e(k) + ce(k-1).$$

To show that $\tilde{u}(k)$ indeed is a stable realization of $u(k)$, we show that there exists parameters c and σ_e^2 such that the right-hand sides have the same auto-correlation functions. The auto-correlation sequence of $e(k) + ce(k-1)$ is

$$\tilde{r}_0 = (1 + c^2)\sigma_e^2, \quad \tilde{r}_1 = c\sigma_e^2, \quad \tilde{r}_l = 0, \ l > 1,$$

and the auto-correlation sequence of $e_1(k) + e_2(k) - ae_2(k-1)$ is

$$r_0 = (1 + a^2)\sigma_2^2 + \sigma_1^2, \quad r_1 = -a\sigma_2^2, \quad r_l = 0, \ l > 0.$$

Setting $\tilde{r}_0 = r_0$ and $\tilde{r}_1 = r_1$ gives $r_0 = (1 + c^2)\sigma_e^2$ and $r_1 = c\sigma_e^2$. Solving for c and σ_e^2 gives the desired result.

References

[1] J. Jonson, J. Jalkanen, L. Johansson, M. Gauss, H. Denier Van Der Gon, Model calculations of the effects of present and future emissions of air pollutants from shipping in the Baltic Sea and the North Sea, Atmos. Chem. Phys. 15 (2) (2015) 783–798.

[2] R. De Waal, A. Bekker, P.S. Heyns, Indirect load case estimation for propeller-ice moments from shaft line torque measurements, Cold Reg. Sci. Technol. 151 (2018) 237–248.

[3] T. Ikonen, O. Peltokorpi, J. Karhunen, Inverse ice-induced moment determination on the propeller of an ice-going vessel, Cold Reg. Sci. Technol. 112 (2015) 1–13.

[4] E. Nestorides, A Handbook on Torsional Vibration, Cambridge University Press, 1958.

[5] L. Meirovitch, Elements of Vibration Analysis, McGraw-Hill Science, Engineering & Mathematics, 1975.

[6] P. Charles, J.K. Sinha, F. Gu, L. Lidstone, A.D. Ball, Detecting the crankshaft torsional vibration of diesel engines for combustion related diagnosis, J. Sound Vib. 321 (3–5) (2009) 1171–1185.

[7] L. Murawski, A. Charchalis, Simplified method of torsional vibration calculation of marine power transmission system, Mar. Struct. 39 (2014) 335–349.

[8] P. Koskinen, M. Jussila, H. Soininen, Propeller Ice Load Models, VTT Technical Research Centre of Finland, 1996.

[9] D. Walker, N. Bose, H. Yamaguchi, S.J. Jones, Hydrodynamic loads on ice-class propellers during propeller-ice interaction, J. Mar. Sci. Technol. 2 (1) (1997) 12–20.

[10] H. Soininen, A Propeller-Ice Contact Model, Technical Research Centre of Finland, 1998.

[11] A. Peddle, J. Dang, T. van Terwisga, Towards a model for propeller-ice interaction, in: International Conference on Offshore Mechanics and Arctic Engineering, Vol. 44939, American Society of Mechanical Engineers, 2012, pp. 395–405.

[12] E.A. Vroegrijk, J.S. Carlton, Challenges in modelling propeller-ice interaction, in: International Conference on Offshore Mechanics and Arctic Engineering, Vol. 45561, American Society of Mechanical Engineers, 2014, V010T07A028.
[13] DNV (Det Norsk Veritas), Ships for navigation in ice, 2016.
[14] Finnish Transport Safety Agency (Trafi), Ice class regulations and the application thereof, 2017, TRAFI/494131/03.04.01.00/2016.
[15] M. Manngård, W. Lund, J. Keski-Rahkonen, J. Nänimäinen, V.-P. Saarela, J. Björkqvist, H.T. Toivonen, Estimation of propeller torque in azimuth thrusters, IFAC-PapersOnLine 52 (21) (2019) 140–145.
[16] J. Glover, The linear estimation of completely unknown signals, IEEE Trans. Automat. Control 14 (6) (1969) 766–767.
[17] B. Friedland, Treatment of bias in recursive filtering, IEEE Trans. Automat. Control 14 (4) (1969) 359–367.
[18] P.K. Kitanidis, Unbiased minimum-variance linear state estimation, Automatica 23 (6) (1987) 775–778.
[19] S. Gillijns, B. De Moor, Unbiased minimum-variance input and state estimation for linear discrete-time systems, Automatica 43 (1) (2007) 111–116.
[20] S. Gillijns, B. De Moor, Unbiased minimum-variance input and state estimation for linear discrete-time systems with direct feedthrough, Automatica 43 (5) (2007) 934–937.
[21] C.-S. Hsieh, Extension of unbiased minimum-variance input and state estimation for systems with unknown inputs, Automatica 45 (9) (2009) 2149–2153.
[22] C.-S. Hsieh, Unbiased minimum-variance input and state estimation for systems with unknown inputs: A system reformation approach, Automatica 84 (2017) 236–240.
[23] R.R. Bitmead, M. Hovd, M.A. Abooshahab, A Kalman-filtering derivation of simultaneous input and state estimation, Automatica 108 (2019) 108478.
[24] E. Lourens, E. Reynders, G. De Roeck, G. Degrande, G. Lombaert, An augmented Kalman filter for force identification in structural dynamics, Mech. Syst. Signal Process. 27 (2012) 446–460.
[25] U. Lagerblad, H. Wentzel, A. Kulachenko, Study of a fixed-lag Kalman smoother for input and state estimation in vibrating structures, Inverse Probl. Sci. Eng. (2020) 1–22.
[26] M. Impraimakis, A.W. Smyth, An unscented Kalman filter method for real time input-parameter-state estimation, Mech. Syst. Signal Process. 162 (2022) 108026.
[27] R. Cumbo, L. Mazzanti, T. Tamarozzi, P. Jiranek, W. Desmet, F. Naets, Advanced optimal sensor placement for Kalman-based multiple-input estimation, Mech. Syst. Signal Process. 160 (2021) 107830.
[28] J. Chauvin, G. Corde, N. Petit, P. Rouchon, Periodic input estimation for linear periodic systems: Automotive engine applications, Automatica 43 (6) (2007) 971–980.
[29] J. Chauvin, G. Corde, P. Moulin, M. Castagné, N. Petit, P. Rouchon, Real-time combustion torque estimation on a diesel engine test bench using time-varying Kalman filtering, in: 2004 43rd IEEE Conference on Decision and Control (CDC)(IEEE Cat. No. 04CH37601), Vol. 2, IEEE, 2004, pp. 1688–1694.
[30] F. Östman, H.T. Toivonen, Model-based torsional vibration control of internal combustion engines, IET Control Theory Appl. 2 (11) (2008) 1024–1032.
[31] G. Genta, Vibration of Structures and Machines: Practical Aspects, Springer Science & Business Media, 2012.
[32] J.P. Den Hartog, Mechanical Vibrations, Courier Corporation, 1985.
[33] W.-K. Ma, T.-H. Hsieh, C.-Y. Chi, DOA estimation of quasi-stationary signals with less sensors than sources and unknown spatial noise covariance: A Khatri-Rao subspace approach, IEEE Trans. Signal Process. 58 (4) (2009) 2168–2180.
[34] T.I. Fossen, T. Perez, Kalman filtering for positioning and heading control of ships and offshore rigs, IEEE Control Syst. Mag. 29 (6) (2009) 32–46.
[35] Det Norske Veritas A.S. (DNV), Ships for navigation in ice: Rules for classification of ships, part 5, chapter 1, 2016.
[36] L. Ljung, A non-probabilistic framework for signal spectra, in: 1985 24th IEEE Conference on Decision and Control, IEEE, 1985, pp. 1056–1060.
[37] T.I. Fossen, Handbook of Marine Craft Hydrodynamics and Motion Control, John Wiley & Sons, 2011.
[38] K.J. Åström, C.G. Källström, Identification of ship steering dynamics, Automatica 12 (1) (1976) 9–22.
[39] K. Zhou, K. Glover, B. Bodenheimer, J. Doyle, Mixed $\mathcal{H}_2$ and $\mathcal{H}_\infty$ performance objectives. I. Robust performance analysis, IEEE Trans. Automat. Control 39 (8) (1994) 1564–1574.
[40] K.J. Åström, Introduction to Stochastic Control Theory, Donver Publications, 2006.
[41] A.H. Sayed, T. Kailath, A survey of spectral factorization methods, Numer. Linear Algebra Appl. 8 (6–7) (2001) 467–496.
[42] M. Verhaegen, V. Verdult, Filtering and System Identification: A Least Squares Approach, Cambridge University Press, 2007.
[43] J.B. Moore, Discrete-time fixed-lag smoothing algorithms, Automatica 9 (2) (1973) 163–173.
[44] B. Anderson, J.B. Moore, Optimal Filtering, Prentice-Hall, 1979, p. 368.
[45] U.S. Paulsen, Performance of meta power rotor shaft torque meter, 2002, pp. 33–41.